

Improved X-ray detection and particle identification with avalanche photodiodes

Marc Diepold,^{1, a)} Luis M. P. Fernandes,² Jorge Machado,^{3, 4} Pedro Amaro,³ Marwan Abdou-Ahmed,⁵ Fernando D. Amaro,² Aldo Antognini,^{6, 7} François Biraben,⁴ Tzu-Ling Chen,⁸ Daniel S. Covita,⁹ Andreas J. Dax,⁷ Beatrice Franke,¹ Sandrine Galtier,⁴ Andrea L. Gouvea,² Johannes Götzfried,¹ Thomas Graf,⁵ Theodor W. Hänsch,^{1, b)} Malte Hildebrandt,⁷ Paul Indelicato,⁴ Lucile Julien,⁴ Klaus Kirch,^{6, 7} Andreas Knecht,⁷ Franz Kottmann,⁶ Julian J. Krauth,¹ Yi-Wei Liu,⁸ Cristina M. B. Monteiro,² Françoise Mulhauser,¹ Boris Naar,⁶ Tobias Nebel,¹ François Nez,⁴ José Paulo Santos,³ Joaquim M. F. dos Santos,² Karsten Schuhmann,^{6, 7} Csilla I. Szabo,^{4, c)} David Taqqu,⁶ João F. C. A. Veloso,⁹ Andreas Voss,⁵ Birgit Weichelt,⁵ and Randolf Pohl¹

¹⁾Max Planck Institute of Quantum Optics, 85748 Garching, Germany.

²⁾LIBPhys, Physics Department, Universidade de Coimbra, 3004-516 Coimbra, Portugal.

³⁾Laboratório de Instrumentação, Engenharia Biomédica e Física da Radiação (LIBPhys-UNL) e Departamento de Física da Faculdade de Ciências e Tecnologia da Universidade Nova de Lisboa, Monte da Caparica, 2892-516 Caparica, Portugal.

⁴⁾Laboratoire Kastler Brossel, UPMC-Sorbonne Universités, CNRS, ENS-PSL Research University, Collège de France, 4 place Jussieu, case 74 75005 Paris, France.

⁵⁾Institut für Strahlwerkzeuge, Universität Stuttgart, 70569 Stuttgart, Germany.

⁶⁾Institute for Particle Physics, ETH Zurich, 8093 Zurich, Switzerland.

⁷⁾Paul Scherrer Institute, 5232 Villigen-PSI, Switzerland.

⁸⁾Physics Department, National Tsing Hua University, Hsincho 300, Taiwan.

⁹⁾i3N, Universidade de Aveiro, Campus de Santiago, 3810-193 Aveiro, Portugal.

(Dated: 28 August 2018)

Avalanche photodiodes are commonly used as detectors for low energy x-rays. In this work we report on a fitting technique used to account for different detector responses resulting from photo absorption in the various APD layers. The use of this technique results in an improvement of the energy resolution at 8.2 keV by up to a factor of 2, and corrects the timing information by up to 25 ns to account for space dependent electron drift time. In addition, this waveform analysis is used for particle identification, e.g. to distinguish between x-rays and MeV electrons in our experiment.

I. INTRODUCTION

Avalanche photodiodes (APDs) are silicon-based solid state detectors that convert photons into a charge current. They provide a compact, robust, magnetic field insensitive solution for light and x-ray detection with gains on the order of 100 and fast response times¹⁻⁴. Due to this, APDs are extensively used in a large variety of physics⁵⁻⁸, medical⁹ and aerospace applications¹⁰.

We have studied x-rays with energies between 1 and 10 keV and observed two distinct APD responses to monoenergetic x-rays absorbed in different depths inside the APD. By constructing APD specific standard traces, and using a pulse-by-pulse fitting technique, we improved the APD energy resolution by a factor of 2, and the time resolution by 30%. In addition, we were able to identify background signals stemming from electrons that deposit a few keV energy in the APD.

The data presented in this work were gathered in the muonic helium Lamb shift experiment^{11,12}, using a set of twenty large area avalanche photo diodes (LAAPDs)

from Radiation Monitoring Devices (model S1315; 13.5 × 13.5 mm² active surface area each). The muonic helium ions represent an extended x-ray source that emits predominantly monoenergetic x-rays of 1.52 keV and 8.22 keV as well as electrons with up to 50 MeV of kinetic energy (see Appendix). Previous tests of these APDs found 40% detection efficiency for 8.2 keV x-rays, and an average energy resolution of 16% (FWHM) after calibration¹³.

Our x-ray detection setup consists of two linear arrays of 10 LAAPDs each, in which each LAAPD is mounted on a separate titanium piece for efficient cooling and easy replacement^{3,13}. The detector arrays are mounted inside a vacuum around 10⁻⁵ hPa, and inside a 5 Tesla magnetic field, above and below the x-ray source. Custom-built low-noise, fast response preamplifiers are fitted to the LAAPDs. Both LAAPD/pre-amplifier assemblies are cooled using an external ethanol circulation system and are actively temperature stabilized at around -30°C. The achieved short term temperature stability was better than ±0.1°C. Highly stable temperatures are crucial for the operation of LAAPDs since their gain depends strongly on their operating temperature^{3,13}. Bias voltages were chosen to provide the best energy resolution per APD and ranged from 1.61 kV up to 1.69 kV, approximately 50 Volts below the breakdown voltage. The pre-amplifiers with two bipolar input transistors in cascode configuration (BFR 182 npn, BFT 92 pnp) have been

^{a)}Corresponding author: marc.diepold@mpq.mpg.de

^{b)}Also at: Ludwig-Maximilians-Universität, 80539 Munich, Germany.

^{c)}Currently at: Theiss Research, 92037 La Jolla, CA USA

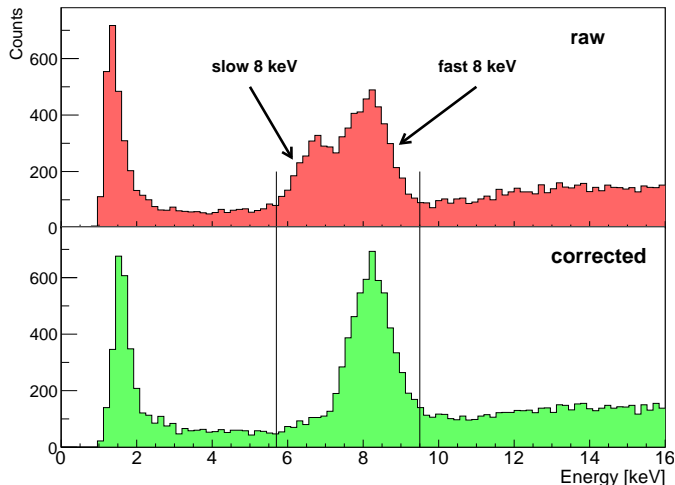


FIG. 1. X-ray energy spectrum from a single APD before (top) and after (bottom) applying our correction. The first spectrum is obtained by integrating over the recorded pulse amplitude in a 200 ns time window after the leading edge. A difference in extracted energy for detector responses with slow and fast rise times (labeled **slow 8 keV** and **fast 8 keV** x-rays respectively) is clearly visible. Improved energy calibration managed to unite both responses and improve the energy resolution by up to a factor of 2 (from 32% to 16% FWHM at 8.2 keV for this APD).

used for the generation of a fast response from the large capacitance (120 pF) of the LAAPD. An overall gain of $150 \text{ mV}/\mu\text{A}$ at 50Ω has been measured with a test pulse. Outgoing APD signals were further amplified by gain 4 main-amplifiers and fed to the CAEN v1720 waveform digitizers (250 MS/s, 12 bit) for recording.

Our experiment requires pileup detection in the x-ray detectors to reduce background effects. Standard shaping amplifiers that are commonly used feature integration times too long to separate pulses on a 100 ns scale. This deteriorated the performance in our previous measurements^{14–16} where we used Rutherford Appleton Laboratory (RAL) 108A pre-amplifiers with μs -long integration times (see¹³ Fig. 16). For our new project^{11,12} we used fast pre-amplifiers with 30 ns rise time. When calculating a simple integral over the recorded pulses, a poor energy resolution became visible as seen in Fig. 1. The double peak structure that was clearly resolved in 6 out of 20 APDs is a result of two different APD responses to the monoenergetic 8.2 keV x-rays as can be seen in the upper part of Fig. 2. Similar effects were previously reported for beveled edge APDs and 14.4 keV x-rays¹⁷. We first observed the same behaviour in a separate test setup without magnetic field. Hence the features described here can not be attributed to magnetic trapping effects in the drift region¹⁸. We can only speculate why this effect was not seen for x-rays taken in another experiment at cryogenic temperatures²¹. Pre-selection of APDs with good

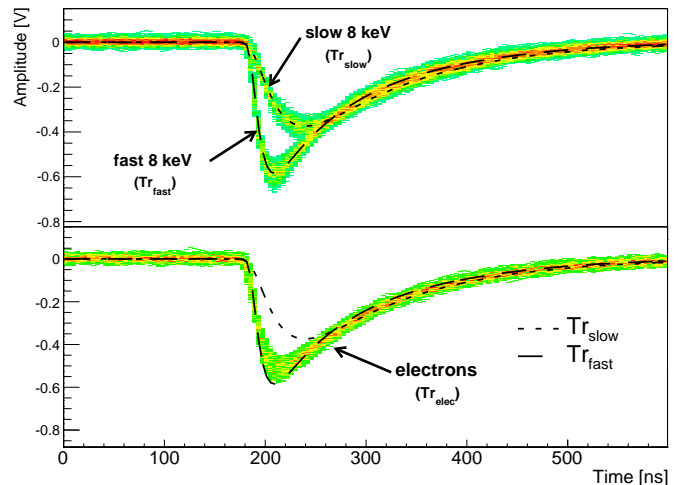


FIG. 2. Top: Typical APD responses for 8.2 keV x-rays. Even though incoming x-rays are quasi mono energetic, the APDs show two distinct responses. The **fast 8 keV** component has a rise time of about 35 ns while the **slow 8 keV** component shows a rise time of about 70 ns. Separate averaging of both individual data sets allows to produce standard traces that accurately describe all x-ray traces between 2 keV and 10 keV. Bottom: Electron induced signals that correspond to an x-ray energy of 8.2 keV after calibration. The dashed curves show the average of the **slow 8 keV** and **fast 8 keV** x-rays. Even though similar in shape to fast 8 keV x-ray signals, a χ^2 fit was able to identify 86% of these electrons correctly.

energy resolution at 5.9 keV can lead to the vanishing of the double peak structure. This was the case in our previous measurement¹³. Also the large average angle of incidence in our setup increases this effect significantly.

To compensate, we developed a simple standard response fitting technique that allowed us to distinguish between different responses on a hit-by-hit basis, improving the energy resolution by a factor of two (see Fig. 1, bottom) and correcting for a 25 ns time shift between both signal types as discussed in Section IV.

In the Secs. II–VI, the different features of the measured x-ray signals are discussed before the fitting routine and the improved energy calibration are presented. Then timing difference between both responses and the influence of electron signals in the analysis are reviewed before a brief summary and outlook is given.

II. APD X-RAY RESPONSE

The working principle of the APDs used in our setup is explained in Fig. 3. In the conversion region (II), incoming photons produce primary photoelectrons. Differences in the thickness of this layer (II) give rise to changes in detector energy acceptance. A p-n junction is placed on the back side of the active volume creating high local

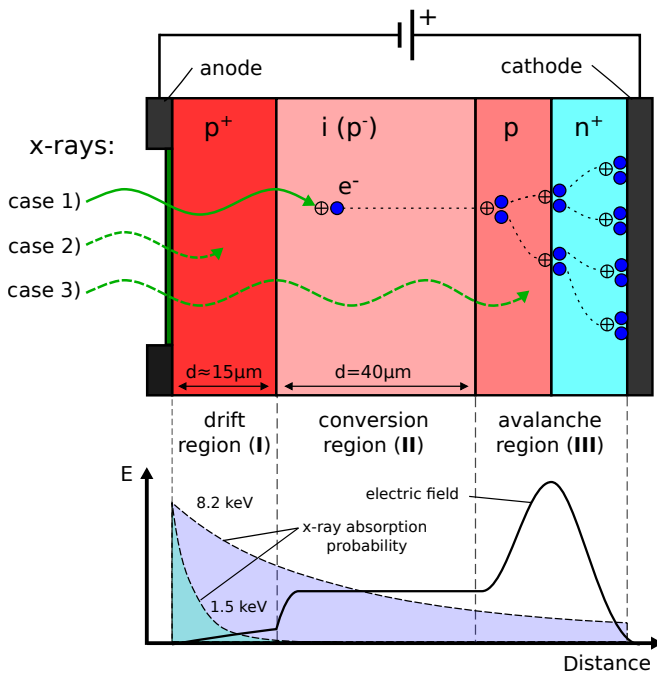


FIG. 3. Working principle of avalanche photodiodes based on a p^+i-p-n^+ doping profile. The weakly doped intrinsic part (**II**) serves as conversion region for most incoming x-rays (case 1). Photoelectrons created are transferred towards the avalanche region. In this high field area secondary electrons are generated through impact ionization providing charge gain. Low energy x-rays have a high probability of being stopped in the initial drift region (**I**) (case 2). These experience additional signal delay and reduced gain. Some photons convert in the multiplication region (**III**), also leading to reduced signal amplitudes (case 3). More about this effect can be found in¹⁷. The bottom figure shows the electric field profile in the several regions of the APD together with the x-ray absorption profile for 1.5 keV and 8.2 keV x-rays.

field strengths. Inside this avalanche region (**III**) electron impact ionization at the high field $p-n^+$ junction leads to a multiplication of free charge carriers providing gain for the initially converted primary photoelectrons². The calculated absorption length for 8.2 keV and 1.5 keV x-rays is $70 \mu\text{m}$ and $9 \mu\text{m}$, respectively¹⁹. Due to the extended size of our x-ray source, the average incident angle of 52 degrees in our geometry gives rise to an effective 1.6 times longer average path inside the APDs. This absorption length for 8 keV x-rays is similar to the APD layer thicknesses and therefore leads to a number of different effects on the APD output depending on the region where the photon is absorbed. The different possibilities are also shown and explained in Fig. 3.

The largest part of the recorded 8 keV x-rays stops in the conversion region (**II**) and follows the normal APD working principle that provides high charge collection efficiency and fast amplification. Nevertheless, some x-rays are absorbed either in the drift layer (**I**) or in the

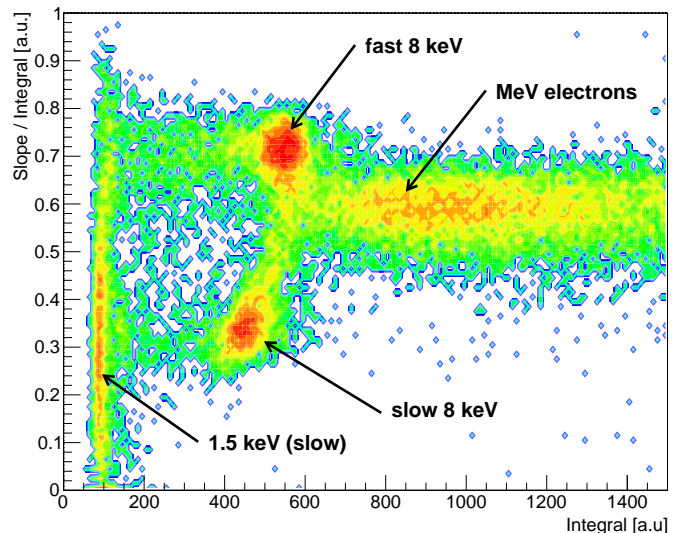


FIG. 4. Normalized slope of the rising edge plotted versus the integral of the pulse. The z-axis (color scale) is logarithmic. Integrals are roughly proportional to the deposited energy of the registered x-rays. Four contributions are visible: Low energy 1.5 keV x-rays show integrals below 200. The recorded 8.2 keV x-rays create two different responses in the APD, one with slow rise time (slope ≈ 0.3), and one with significantly faster rise time (slope ≈ 0.7). The last contribution with an integral above 700 arises from MeV electrons depositing keV energy in the APD active region.

avalanche region (**III**). The x-rays absorbed in region (**III**) undergo only partial amplification resulting in low amplitudes down to zero. This gain reduction is responsible for the flat energy tails seen in Fig. 1. X-rays absorbed in region (**I**) generate electrons which are only slowly transferred to the following region (**II**) due to the lower field strengths in (**I**). Traps in this region may hold electrons for non-negligible times, lengthening the pulse and causing a reduction in amplitude¹⁷ (see Fig. 2). Similar effects of reduced charge collection efficiency were also studied for x-ray energies below the silicon K-edge²⁰. From Fig. 2 we also observe that these x-rays only show a single amplitude and not a continuous distribution up to the one of x-rays absorbed in region (**II**). This indicates that the trapping mechanism occurs at the boundary between regions (**I**) and (**II**).

III. X-RAY ENERGY DIFFERENCES AND COMPENSATION

In order to investigate this effect a set of roughly 2.5×10^4 x-ray traces were recorded per APD. Fitted baseline fluctuations were below 10 mV for all analyzed signals, compared to average signal amplitudes of 500 mV for 8.2 keV x-rays.

Our analysis routine starts with an edge finder (square

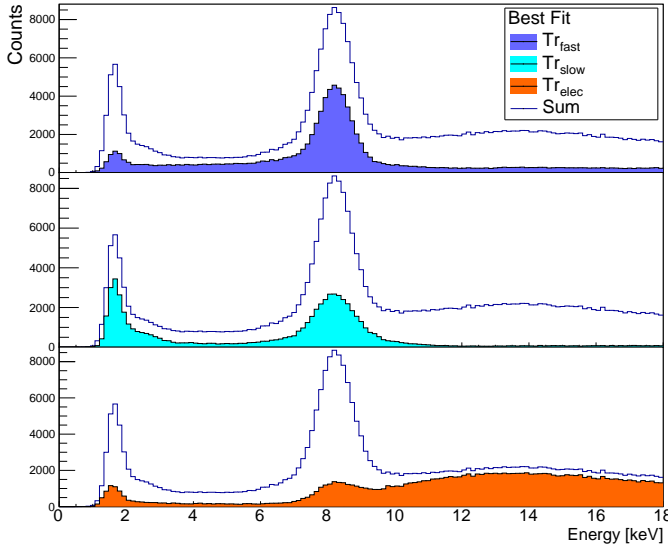


FIG. 5. Energy spectra of recorded x-rays and electrons in the muonic helium Lamb shift experiment categorized by the standard trace which provides the lowest χ^2 in a range of 200 ns after the leading edge of the pulse. All spectra show two prominent peaks at 1.5 keV and 8.2 keV. The fast rising component provided by $\mathbf{Tr}_{\text{fast}}$ in dark blue unfolds signals converted in or behind the conversion region (II). It consists mostly out of 8.2 keV x-rays and the visible low energy tail is created by the loss of gain for x-rays converted in the avalanche region (III). The light blue distribution stands for all traces that were best described by the slow rising pulse shape $\mathbf{Tr}_{\text{slow}}$ and consists mostly out of 1.5 keV x-rays and some 8.2 keV x-rays mixed in. Signals best matching the electron trace $\mathbf{Tr}_{\text{elec}}$ are shown in the orange division. These signals are formed by a continuous electron background and a contribution of wrongly identified x-rays.

weighting function with a width of 200 ns) to find the beginning of the pulse in the recorded trace. Then the slope of the leading edge is fitted with a linear function. Using a χ^2 criterion we improve the accuracy of the slope determination by varying start time of the pulse within 20 ns while keeping the fitting window fixed. Finally, we normalize the slope to the pulse integral provided by the edge finder to obtain the (amplitude-independent) rise time of the pulse.

When the rise time is plotted versus the integral of the pulse, four different contributions to the spectra can be identified as seen in Fig. 4. The two most prominent peaks are created by converted 8.2 keV photons with slow and fast detector responses, labeled **slow 8 keV** and **fast 8 keV** respectively. For these peaks we see a clear difference in rise time and integral while most of the low energy 1.5 keV x-rays show a slow rise time. The rise time distribution for small signals is broadened due to low amplitudes and noise.

The last visible component is generated by the already mentioned high energy (up to 50 MeV) electrons

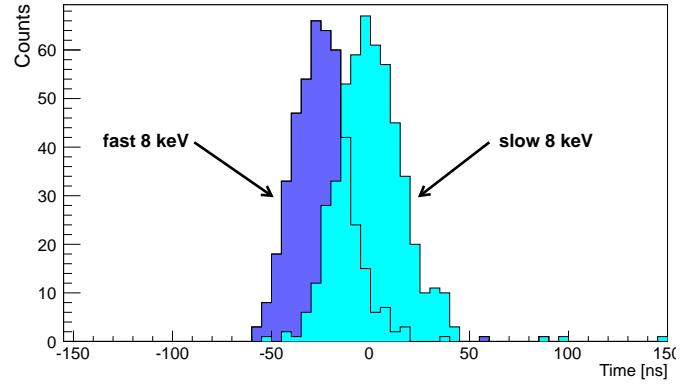


FIG. 6. Spectra showing the relative timing between **slow 8 keV** and **fast 8 keV** x-rays for a single APD. These time spectra have been obtained by plotting the time of the 8.2 keV x-ray signal detected in a LAAPD relative to the 1.5 keV signal detected in another LAAPD for both classes. Both LAAPDs including preamp-delay line etc. have been synchronized using electrons. The origin is chosen as the center of gravity of the **slow 8 keV** response. A 25 ns timing difference could be measured between both responses. The relatively poor time resolution is given by the coincident 1.5 keV x-rays that are detected just above the noise level in our setup leading to a washed out signal.

(created by muon-decay, further explained in the appendix). These electrons deposit energies up to 50 keV in the APDs and their signals display a third kind of standard pulse shape, namely a mixture of fast and slow x-ray pulse shapes. This is shown in the lower panel of Fig. 2.

In order to further analyze the two classes of 8.2 keV x-rays, two sets of APD traces for **slow 8 keV** and **fast 8 keV** were created by selecting the respective peaks in Fig. 4 with adequate cuts. A collection of selected traces for the **slow 8 keV** and **fast 8 keV** cases is shown in Fig. 2. For each of the two x-ray classes, traces were numerically averaged after shifting each trace to correct for the variation of the pulse starting time. This averaging created the standard traces of the subsets ($\mathbf{Tr}_{\text{slow}}$ & $\mathbf{Tr}_{\text{fast}}$). These traces had to be produced once per each APD for a measurement period of several months and stayed constant throughout multiple heating/cooling cycles of the APD assembly.

For the final analysis, each APD pulse is fitted with all available standard traces. Starting at the time provided by the edge finder, the standard trace is fitted to the pulse. The timing is then varied and the χ^2 is recorded for each fit. To save computational effort that would arise for a 2-parameter fit (amplitude and time), the amplitude of the standard trace is always fixed by matching its integral to the integral of the signal (after baseline subtraction) in a 200 ns wide time window.

Finally, the minimal χ^2 between the various standard traces is used to separate the pulses into different classes:

slow 8 keV and **fast 8 keV** (and electrons, see below). The result from the best-fitting class is used to get amplitude, integral and timing values of the recorded signal.

The allocation of the recorded APD signals in the **slow 8 keV** and **fast 8 keV** classes according to the fit routine can be seen in the top parts of Fig. 5. Calibration of the two x-ray spectra created by the $\mathbf{Tr}_{\text{slow}}$ and $\mathbf{Tr}_{\text{fast}}$ fits is done by matching the peaks in both separate integral spectra to the respective energy of 8.2 keV. As expected, the **fast 8 keV** component of x-rays is the largest part of the recorded signals in our setup as seen in Fig. 5. The observed 1:1.7 ratio of **fast 8 keV** to **slow 8 keV** x-rays agrees roughly with the expected absorption ratio of 1:1.5 estimated from the thicknesses of layers (I) and (II).

IV. X-RAY TIMING DIFFERENCES

In addition to the variation in the observed 8.2 keV x-ray energy we were also able to measure a difference in timing between the **fast 8 keV** and the **slow 8 keV** components.

In order to achieve a common timing reference point for this study, coincidence events between the 8 keV x-rays recorded in the APD under investigation and the 1.5 keV x-rays registered in neighboring APDs were studied. These two x-ray types are emitted within a picosecond time window from the muonic atoms used (as is further explained in the appendix).

Special attention was given to time calibration in order to avoid possible timing shifts created by the distinct standard traces $\mathbf{Tr}_{\text{fast}}$ and $\mathbf{Tr}_{\text{slow}}$ used for different signals. Therefore calibration of the different APDs and traces against each other was done using the supplementary measured electron signals. The MeV electrons create hits in multiple detectors on their spiraling motion in the surrounding magnetic field enabling us to get a common timing for all APDs.

When comparing the timing of the measured 8.2 keV x-rays we observed a 25 ns delay between **slow 8 keV** signals and normal **fast 8 keV** signals. A time spectrum showing this effect for a single APD is shown in Fig. 6. Correcting for this effect improves the APD time resolution of our setup by more than 30% when the two responses seen in Fig. 6 are unified. Better results might be achieved when a more clearly defined common timing is provided since the timing resolution is limited by the low amplitude 1.5 keV signals just above the noise level.

V. MeV ELECTRON DETECTION WITH APDS

Apart from the improved energy resolution that was achieved with the methods described in Section III, we were also able to differentiate high energy electron signals in the APDs from similar x-ray signals. These MeV electrons deposit up to 50 keV in the APD active volume

and were always present in the experiment. Due to their passage through all the APD layers, electrons show signals with yet another shape that can be distinguished from the previously discussed **fast** and **slow** x-ray responses. A third standard trace $\mathbf{Tr}_{\text{elec}}$ was created by averaging a set of clearly identified electron signals that correspond to a mean energy of 12 keV. This was done supplementary to the already known x-ray traces $\mathbf{Tr}_{\text{slow}}$ and $\mathbf{Tr}_{\text{fast}}$. A comparison of an electron induced signal shape at 8.2 keV and the respective real x-ray traces is also shown in Fig. 2 (bottom). As electrons with MeV energies deposit energy in all three APD layers. (I, II, III). The corresponding standard trace $\mathbf{Tr}_{\text{elec}}$ can be approximately parameterized as a mixture of the $\mathbf{Tr}_{\text{slow}}$ and $\mathbf{Tr}_{\text{fast}}$ standard responses. Using the same routine as for the previous pulse analysis, the fit was able to differentiate between x-ray and electron signals with very high fidelity, leading to a correct electron identification in 86% of the cases.

VI. SUMMARY

We have observed effects from the APD layer structure that lead to two distinct responses to X-rays in the 6-10 keV range. The individual signal types can be identified with high fidelity by examining the rising edge of the measured pulses. Correcting for this effect improves the energy resolution by up to a factor of 2 depending on the APD. Additionally we were able to correct for timing differences between both responses. While the different rise time classes were observed in all 20 APDs under investigation, only 6 of them showed a resolved double-peak structure in the energy spectrum obtained by a simple integral.

Using the rise time analysis, it was also possible to filter MeV energy decay electrons. An electron-specific standard trace was clearly distinguishable from the two different kinds of x-ray signals recorded for 8.2 keV x-rays. A χ^2 fit of the signal shape was used to exclude them from the x-ray data with an overall effectiveness of 86%, while only 14% of the 8 keV x-rays were wrongly identified as electrons. This led to significant background reduction in the μHe Lamb shift experiment^{11,12}.

ACKNOWLEDGMENTS

We thank Ulf Röser, Matteo Nüssli, Hanspeter v. Gunten, Werner Luster, Adamo Gendotti, Florian Barchetti, Ben van den Brandt, Paul Schurter, Michael Horisberger and the MPQ, PSI, ETH Workshops and support groups for their help. M.D., B.F., J.J.K., F.M. and R.P. acknowledge support from the European Research Council (ERC) through StG. #279765. F.D.A., L.M.P.F., A.L.G., C.M.B.M. and J.M.F.S. acknowledge support from FEDER and FCT in the frame of project PTDC/FIS-NUC/0843/2012.

C.M.B.M. acknowledges the support of FCT, under Contract No. SFRH/BPD/76842/2011. F.D.A. acknowledges the support of FCT, under Contract No. SFRH/BPD/74775/2010. A.A, K.K and K.S acknowledge support from SNF 200021L-138175. T.G., A.V., B.W and M.A.A. acknowledge support of DFG.GR.3172/9-1. This research was supported in part by Fundação para a Ciência e a Tecnologia (FCT), Portugal, through the projects No. PEstOE/FIS/UI0303/2011 and PTDC/FIS/117606/2010, financed by the European Community Fund FEDER through the COMPETE. P. A. and J. M. acknowledges the support of the FCT, under Contracts No. SFRH/BPD/92329/2013 and SFRH/BD/52332/2013.

Appendix: The μHe Lamb shift experiment

The data presented in this work were acquired using muonic helium ions as x-ray source during the recent μHe Lamb shift experiment^{11,12}. The experiment is performed at the high intensity proton accelerator facility at Paul Scherrer Institute in Switzerland. Its' purpose was to measure the different $2S \rightarrow 2P$ transitions in the $\mu^4\text{He}^+$ and $\mu^3\text{He}^+$ exotic ions via laser spectroscopy. The required information about its environment and working principle will be briefly sketched in this section.

The accelerator physics environment leads to stringent demands on stability and robustness of the APDs and the analysis routine employed that exceed common specifications. For example, the APD arrays used are placed inside a 5 T solenoidal magnet where they are mounted next to a low pressure helium gas target. Muonic ions are created in this 20 cm long gas volume operated at 2 – 4 hPa by low energy muons that are provided by the accelerator beam line. The dataset described in this work was obtained during the $\mu^4\text{He}^+$ measurement campaign in 2013 that offers multiple transitions in the low keV x-ray region. These consist of the L_α , L_β and L_γ transitions at 1.52 keV, 2.05 keV and 2.30 keV respectively as well as the K_α , K_β and K_γ transitions at 8.22 keV, 9.74 keV and 10.28 keV, emitted by the muonic helium ions during the so-called atomic cascade within a time frame of few ns total²².

The muons decay after an average lifetime of 2.2 μs into muon neutrino, electron antineutrino and "high energy" electrons in the MeV range. These electrons deposit energy when transversing the APD, creating electron hole pairs in all regions of the APD quasi simultaneously. The induced signals correspond to virtual x-ray energies of up to 50 keV. This would raise background effects for the experiment that uses the recorded 8.2 keV $\mu^4\text{He}^+$ K_α x-rays as signal for laser spectroscopy. Therefore a supplemental set of 4 plastic scintillators surrounds the gas target and APD arrays for additional means of electron

detection and exclusion of background. Since the overall detection efficiency for electrons in the mentioned plastic scintillators is only roughly 30 %, additional means for electron identification were desirable. This was achieved by waveform analysis described in Sections III and V.

- ¹J. Kataoka et al., Recent progress of avalanche photodiodes in high-resolution X-rays and γ -rays detection Nucl. Instrum. Meth. A 541, 398 (2005).
- ²D. Renker and E. Lorenz, Advances in solid state photon detectors, JINST 4, p. P04004 (2009).
- ³L. M. P. Fernandes et al., Characterisation of large area avalanche photodiodes in X-ray and VUV-light detection, JINST 2, P08005 (2007).
- ⁴L. M. P. Fernandes et al., Behaviour of large-area avalanche photodiodes under intense magnetic field for VUV- visible and X-ray photon detection, Nucl. Instrum. Meth. A 498, 362 (2003).
- ⁵S. Tanaka et al., Development of wideband X-rays and γ -rays spectrometer using transmission-type, large-area APD, Nucl. Instrum. Meth. A 582, 562 (2007).
- ⁶S. Kasahara et al., Variability of the minimum detectable energy of an APD as an electron detectors, Nucl. Instrum. Meth. A 664, 282 (2012).
- ⁷D. Renker, Properties of avalanche photodiodes for applications in high energy physics, astrophysics and medical imaging Nucl. Instrum. Meth. A 486, 164 (2002).
- ⁸R. Lecomte et al., Initial results from the Sherbrooke avalanche photodiode positron tomograph, IEEE Trans. on Nucl. Sci. 43, 3 (2002).
- ⁹C. Marriott et al., High-resolution PET imaging and quantitation of pharmaceutical biodistributions in a small animal using avalanche photodiode detectors, Journ. Nucl. Med. 35(8), 1390 (1994).
- ¹⁰T. Toitumi et al., In-orbit performance of avalanche photodiode as radiation detector onboard a pico-satellite Cute-1.7+APD II Journal of Geophysical Research, 115, A05204 (2010).
- ¹¹A. Antognini et al., Illuminating the proton radius conundrum: the muonic helium Lamb shift Can. J. Phys. 89, 47 (2011).
- ¹²T. Nebel et al., The Lamb-shift experiment in muonic helium, Hyp. Int. 212, 195 (2012).
- ¹³L. Ludhova et al., Planar LAAPDs: temperature dependence, performance, and application in low energy xray spectroscopy, Nucl. Instrum. and Meth. A 540, 169 (2005).
- ¹⁴R. Pohl et al., The size of the Proton, Nature 466, 213 (2010).
- ¹⁵A. Antognini et al., Proton structure from the measurement of 2S-2P transitions frequencies of muonic hydrogen, Science 339, 417 (2013).
- ¹⁶M. Diepold et al., Lifetime and population of the 2S state in muonic hydrogen and deuterium, Phys. Rev. A 88, 042520 (2013).
- ¹⁷A.Q.R. Baron and S.L. Ruby, Time resolved detection of x-rays using large area avalanche photodiodes, Nucl. Instrum. and Meth. A 343 517 (1994).
- ¹⁸T.R. Gentile et al., Magnetic field effects on large area avalanche photodiodes at cryogenic temperatures, Nucl. Instrum. and Meth. A 652 520 (2011).
- ¹⁹See <http://physics.nist.gov/PhysRefData/FFast/html/form.html> for x-ray penetration depths in silicon.
- ²⁰T. R. Gentile et al., Response of large area avalanche photodiodes to low energy x rays, Rev. Sci. Instrum. 83, 053105 (2012).
- ²¹R.I. Cooper et al., A gamma- and X-ray detector for cryogenic, high magnetic field applications. Nucl. Instrum. and Meth. A 691 64 (2012).
- ²²G. Reifenröther et al., Cascade of muonic helium ions, Phys. Lett. B. 191, 15 (1987).